Exciton Dynamics in Suspended Monolayer and Few-Layer MoS_2 2D Crystals

Hongyan Shi,[†,‡] Rusen Yan,[§] Simone Bertolazzi,[⊥] Jacopo Brivio,[⊥] Bo Gao,[‡] Andras Kis,[⊥] Debdeep Jena,[§] Huili Grace Xing,[§] and Libai Huang[†,*]

[†]Radiation Laboratory and [§]Department of Electrical Engineering, University of Notre Dame, Notre Dame, Indiana 46556, United States, [‡]Department of Physics, Harbin Institute of Technology, Harbin, China, and [⊥]Electrical Engineering Institute, Ecole Polytechnique Federale de Lausanne(EPFL), CH-1015 Lausanne, Switzerland

ABSTRACT Femtosecond transient absorption spectroscopy and microscopy were employed to study exciton dynamics in suspended and Si_3N_4 substrate-supported monolayer and few-layer MoS_2 2D crystals. Exciton dynamics for the monolayer and few-layer structures were found to be remarkably different from those of thick crystals when probed at energies near that of the lowest energy direct exciton (A exciton). The intraband relaxation rate was enhanced by more than 40 fold in the monolayer in comparison to that observed in the thick crystals, which we attributed to defect assisted scattering. Faster electron–hole recombination was found in monolayer and few-layer structures due to quantum confinement effects that lead to an indirect–direct band gap crossover. Nonradiative rather than radiative relaxation pathways dominate the dynamics in the monolayer and few-layer MoS_2. Fast trapping of excitons by surface trap states was observed in monolayer and few-layer structures, pointing to the importance of controlling surface properties in atomically thin crystals such as MoS_2 along with controlling their dimensions.

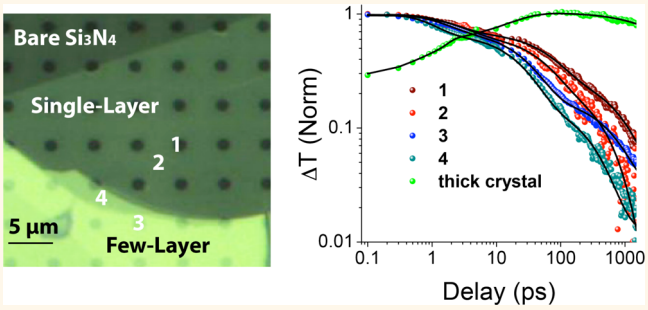

KEYWORDS: MoS_2 · atomically thin 2D crystal · exciton dynamics · transient absorption spectroscopy · transient absorption microscopy · quantum confinement · surface defects

Transition metal dichalcogenides are layered materials where the adjacent planes are held together by van der Waals interactions.[1,2] These weak interlayer interactions allow for micromechanical exfoliation of single layers from bulk crystalline samples similar to the fabrication of graphene from graphite.[2] Single layers of transition metal dichalcogenides can be either semiconducting or metallic depending on the structure.[1,2] In particular, MoS_2 has recently emerged as a promising candidate for the semiconducting analogue of graphene.[2–6] Field-effect transistors have been successfully fabricated from monolayer and few-layer MoS_2 samples with performance which rivals that of those from graphene ribbons.[3]

Quantum confinement effects are expected to be important for monolayer and few-layer MoS_2 structures because the thickness becomes smaller than the exciton Bohr radius.[2,7–10] A recent computational work predicted the Bohr radius for monolayer MoS_2 to be 0.93 nm with a large exciton bing energy of ~0.9 eV.[9] Unlike that of a conventional bulk semiconductor, interlayer interaction in layered structures modifies excitonic properties in a complex manor.[9] Indeed, a dramatic enhancement of photoluminescence quantum efficiency in monolayer MoS_2 has been observed in photoluminescence (PL) experiments and was attributed to indirect–direct band gap crossover in the monolayer due to such quantum confinement effects.[11,12] More recently, long-lived (>1 ns) valley polarization was observed in monolayer MoS_2.[13,14]

While the steady-state optical spectroscopy of MoS_2 2D crystals has been reported,[1,15,16] very limited work has been done on ultrafast time-resolved spectroscopy of this system.[17–19] Recent temperature-dependent PL lifetime measurements provided important information on exciton lifetimes in monolayers.[17] Transient absorption

* Address correspondence to lhuang2@nd.edu.

Received for review August 29, 2012 and accepted December 29, 2012.

Published online 10.1021/nn303973r

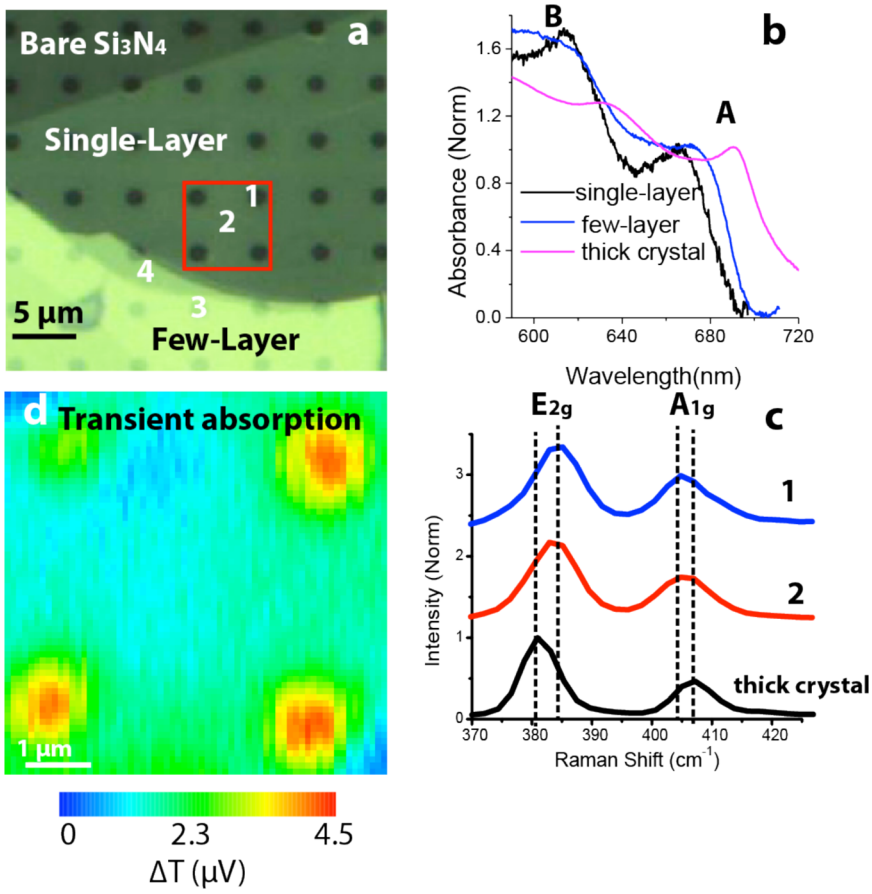

Figure 1. (a) An optical micrograph of the sample investigated. The red square marks the area imaged in panel d. The four positions studied in detail are as marked: suspended single-layer (1), supported single-layer (2), suspended few-layer (3), and supported few-layer (4). (b) Normalized ground state absorption of positions 1 and 3 in comparison to the thick region. A and B denote the two lowest energy direct excitons. (c) Raman spectra of positions 1 and 2 and the thick crystal. (d) Transient absorption image at 0 ps for the area as marked by the red square in panel a. The red color represents high ΔT value while blue is a low ΔT value.

spectroscopy of few-layer MoS_2 has also been recently reported.[18,19] However, questions have remained about quantum confinement and environmental effects on relaxation pathways as the thickness is progressively reduced to the monolayer level. Understanding the nature of the excited states and time scales for the different relaxation processes in relation to their reduced dimensionalities is of key importance for realizing applications of these novel materials. In addition, being single layer thick with essentially all atoms on the surface, both surface defects and the nature of the substrate can play critical roles in modulating excited state dynamics.

Here we present a study on exciton dynamics in monolayer and few-layer crystals, as well as in thick crystals, to elucidate thickness-dependent exciton relaxation pathways. Exciton dynamics in monolayer and few-layer samples were significantly different from those in the thick crystals, and enhanced intraband and interband relaxation rates were observed in both monolayer and few-layer cases. Our experimental observations demonstrated that both surface defects and quantum confinement effects play pivotal roles in determining the exciton dynamics in monolayer and few-layer MoS_2.

RESULTS AND DISCUSSION

The optical micrograph shows regions with different contrast due to optical interference, which allows for fast identification of sample thickness.[20] As seen in Figure 1a, the sample contains both monolayer and few-layer regions. Microscopy (AFM) height measurement (Figure S1 in Supporting Information) taken before the transfer process confirms the monolayer region as marked in Figure 1a has a thickness of 0.8 nm. The AFM image shows that the monolayer suspended over the holes (Supporting Information, Figure S2) is lower in height due to adhesion to the side-wall of the hole indicating that the monolayer is freely suspended.[21] For the following discussion, we focus on optical spectroscopy and dynamics taken at four different positions as marked in Figure 1a: suspended single-layer (1), supported single-layer (2), suspended few-layer (3), and supported few-layer (4). From Raman measurements, the few-layer region was estimated to be 4–5 layers thick.[22–27] For comparison, a much thicker region where no quantum confinement was evident in ground-state absorption spectra (hereafter denoted as thick crystal) was also studied. With a

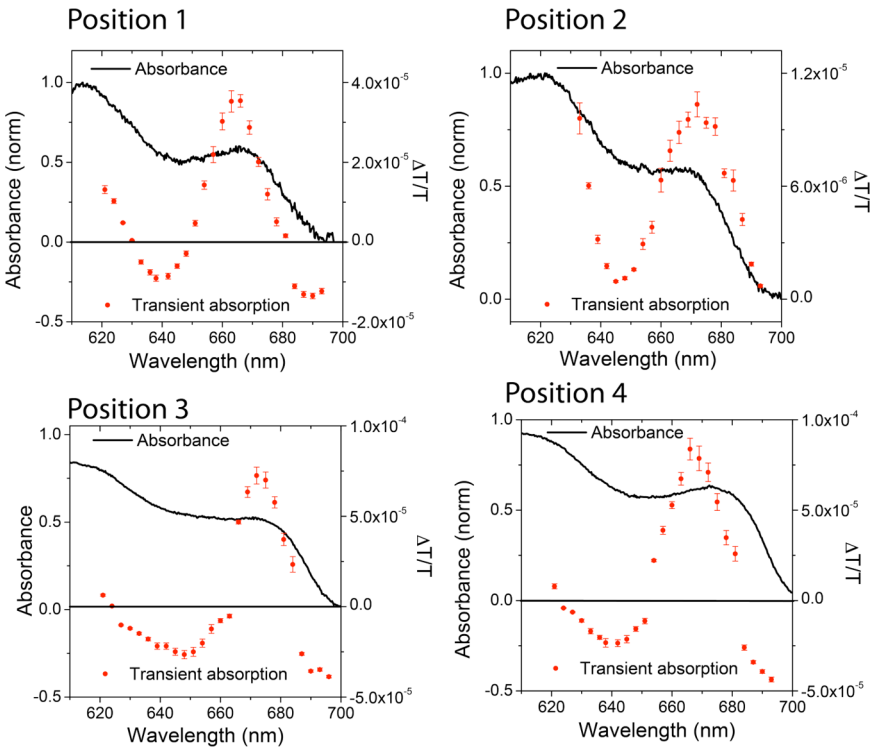

Figure 2. Transient absorption spectra at 0 ps delay (red dots) and ground-state absorption spectra (black lines) for positions 1, 2, 3, and 4. Pump wavelength is at 387 nm and pump fluence is 1.3 μJ/cm^2. Probe fluence is 3.7 μJ/cm^2.

transmission of ~10%, the thickness of this thick crystal is estimated to be ~100 nm (or ~150 layers) by using an absorption coefficient of 10^5 cm^{-1} as given by ref 28.

Figure 1b shows ground-state absorption spectra for the monolayer and the few-layer positions in comparison to the thick crystal measured by reflectance spectroscopy. The spot size of the white light used for acquiring ground-state absorption spectra is ~1 μm, larger than the laser spot size of ~400 nm employed in the pump–probe measurements described later. The two absorption peaks in the spectral range of 600–700 nm correspond to A and B excitons as labeled. The A and B excitons associated with direct transitions from a split valence band resulting from spin–orbit splitting in the MoS_2 interlayer interaction further modifies this split.[9,15] For the monolayer and the few-layer, A and B exciton energy levels blue-shift due to quantum confinement effects as the thickness of the crystals decreases. This is in agreement with previous reports.[1,28,29] Raman spectra (Figure 1c) show two prominent features corresponding to the E_{2g} and A_{1g} bands. The monolayers (positions 1 and 2) exhibit an upshift of E_{2g} band frequency and a downshift of A_{1g} band frequency when compared to the thick region, again consistent with previous reports.[23]

To resolve how reduced dimensionality and the environment affect exciton dynamics, transient absorption spectroscopy and imaging measurements were performed on sample positions with different thickness. Note that all measurements presented in this manuscript were carried out at room temperature. As an example, a transient absorption microscopy (TAM) image at 0 ps delay of the monolayer area as marked by the red square in Figure 1a is illustrated in Figure 1d. The TAM image plots pump-induced change in probe transmission (ΔT) values as recorded by the lock-in amplifier. For TAM imaging, the pump wavelength was set at 387 nm while a probe wavelength of 670 nm was chosen to be resonant with the A exciton. The TAM image clearly shows the suspended areas with higher signal level (ΔT). This is due to higher transmission (T) in the suspended areas resulting from the lack of a substrate. Therefore the spatial resolution of these experiments is sufficient to differentiate the suspended areas from the substrate-supported areas.

Transient absorption spectra at 0 ps delay time along with steady state absorption spectra for positions 1, 2, 3, and 4 are illustrated in Figure 2. A pump wavelength at 387 nm (3.2 eV) created photoexcited electron–hole pairs at the C excitonic level.[1] These high-energy electrons and holes consequently decayed to lower energy levels through intraband relaxation.[30] Dynamics near the A exciton were monitored by tuning the probe wavelength between 600 and 700 nm. A pump fluence of 1.3 μJ/cm^2 and a probe fluence of 3.7 μJ/cm^2 were employed to acquire these spectra. By using an absorption coefficient of 10^5 cm^{-1} from ref 28 and a monolayer thickness of 0.65 nm, a pump fluence of 1.3 μJ/cm^2 corresponds to a photoexcited carrier density of ~1.6 × 10^{10} /cm^2 per layer.

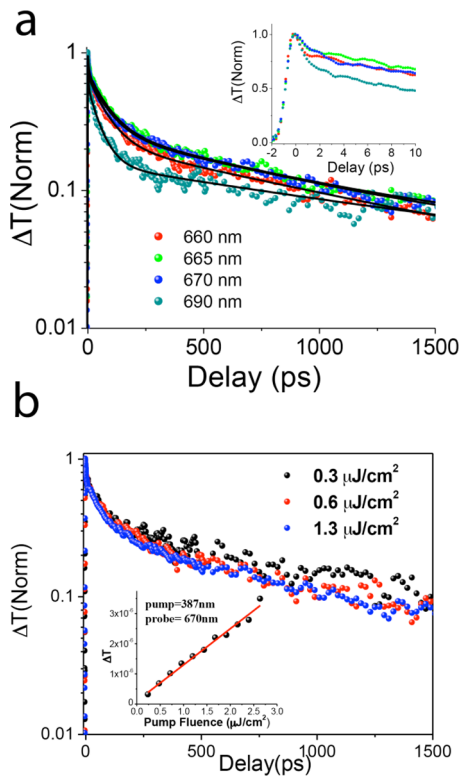

Figure 3. (a) Transient absorption dynamics for suspended monolayer (position 1) with a pump wavelength of 387 nm and probe wavelengths as marked. The solid lines are fits of a triexponential decay function convoluted with a Gaussian response function. Inset is the zoom in for the first 10 ps. (b) Transient absorption dynamics for a probe wavelength of 670 nm at different pump fluences for a suspended monolayer (position 1). Inset plots ΔT as a function of pump fluence. The solid line is a linear fit.

For all four positions, photoinduced bleach (PB, positive ΔT) bands near the A exciton resonance were observed, which can be understood as a band filling effect.[31] Photoinduced absorption (PA, negative ΔT) bands were also observed for positions 1, 3, and 4. These PA bands are symmetrically situated on both sides of the PB bands, suggesting a carrier-induced peak broadening mechanism.[32] Notably, for position 2 (supported monolayer) no obvious PA bands were observed. Doping effects introduced by the substrate could explain this result if the minority carrier has stronger PA signals. Further experiments are needed to explore these effects.

Figure 3a presents dynamics for the suspended monolayer (position 1) taken at a range of probe wavelengths with a fixed pump wavelength of 387 nm and a pump fluence of 1.3 μJ/cm^2, the same condition as described for Figure 2. The probe fluence used is 3.7 μJ/cm^2. We have found that dynamics exhibited no dependence on probe intensity in the range of 0.5−4 μJ/cm^2. We have taken dynamics at multiple suspended monolayer positions and the results are included in Figure S5 of the Supporting Information. No major difference in dynamics was observed for different suspended monolayer positions. The inset of Figure 3a zooms in on the dynamics of the first 10 ps. All curves exhibit an instantaneous rise within the pulse width of ~500 fs. Kinetics taken at all probe wavelengths exhibit multiexponential decays and can be fitted using a Gaussian response function convoluted with a triple exponential decay function of $Ae^{-t/\tau_1} + Be^{-t/\tau_2} + Ce^{-t/\tau_3}$ (Figure 3a), where $\tau_1 < \tau_2 < \tau_3$. Supporting Information, Table S1 lists the fitting parameters for the decay curves displayed in Figure 3a. For both the PB (660, 665, and 670 nm) and PA (690 nm) bands, similar values of τ_1, τ_2, and τ_3 are obtained indicating that the PA and PB bands result from the same processes, consistent with a carrier-induced broadening mechanism. When probing resonantly at the A exciton (670 nm), the resulting decay time constants are 2.6 ± 0.1 ps (τ_1), 74 ± 3 ps (τ_2), and 850 ± 48 ps (τ_3), respectively. Further discussion on the origins of these decay times will be presented later in the discussion.

Intensity dependence of the dynamics taken at 670 nm for position 1 (suspended monolayer) and position 2 (supported monolayer) is illustrated in Figure 3b and Supporting Information, Figure S6, respectively. No significant pump intensity dependence was observed, suggesting that higher order processes such as exciton−exciton annihilation were negligible for the pump intensities employed in our experiments. Also, the lack of pump intensity dependence implies that a hot phonon effect is not significant at the pump fluences employed in these measurements.[30] ΔT at zero time delay *versus* pump fluence for position 1 is shown in the inset of Figure 3b, where a linear relationship was observed, indicating that the optical transitions are not saturated in these experiments. Such a linear dependence on pump intensity was observed for all sample positions investigated.

Next we compare exciton dynamics for sample positions with different thicknesses. We chose to probe exciton dynamics at the A exciton resonance where maximum pump-induced absorption changes occur. Figure 4 depicts the dynamics when probing at the A exciton resonance (670 nm) for the monolayer and few-layer positions as well as dynamics from the thick crystal, probing close to its A exciton resonance (690 nm). Figure 4a is presented in semilog scale and Figure 4b is plotted in log−log scale. The decay curves were fitted with the triexponential decay function as described earlier. The fitting parameters for the decay curves displayed in Figure 4 are summarized in Table 1. Most interestingly, the dynamics of the thick crystal were remarkably different from those of the monolayer and the few-layer cases. As more clearly shown in Figure 4b, the signal at the thick crystal exhibits a biexponential rise with time constants of 1.8 ± 0.6 ps (19% of weight) and 20 ± 2 ps (81% of weight), contrary to the instantaneous (<500 fs) rise at the

monolayer and few-layer positions. After the initial rise, the dynamics in the bulk decay with a single exponential decay of 2626 ± 192 ps, which is also different than the triexponential decay behavior found at the monolayer and the few-layer positions.

In the following, we discuss possible processes contributing to the dynamics observed. In principle, thermal effects can also play a role; however, the increase of the lattice temperature induced by the pump irradiation is minimal, on the order of ~0.1K for the highest pump intensity of 1.3 μJ/cm^2, using a heat capacity of 1.89 J cm^{-3} K^{-1} as reported in ref 33. We note that the high repetition rate of the laser system could have led to heat accumulation if the time between pulses of 13 ns is not long enough for efficient heat dissipation. However, for the pump intensities ($\leq$1.3 μJ/cm^2) we employed in these experiments, such heat accumulation is negligible as demonstrated by the lack of pump intensity dependence in the relaxation dynamics for both the suspended and the supported regions (Figure 3b and Supporting Information, Figure S6). If thermal effects would be significant, one would expect pump intensity dependence of the dynamics for the suspended region to be different from the supported region because heat dissipation is slower for the suspended region. Specifically, dynamics would become slower at higher pump intensities if heat accumulation would be significant, and this effect would be more pronounced in the suspended monolayer than in the supported monolayer. But this is not what we observed; for both the suspended and the supported regions, dynamics are essentially independent of pump intensities under our experimental conditions. We therefore conclude that electronic relaxation rather than thermal dissipation dominates the dynamics observed in our experiments and discuss our results in these terms.

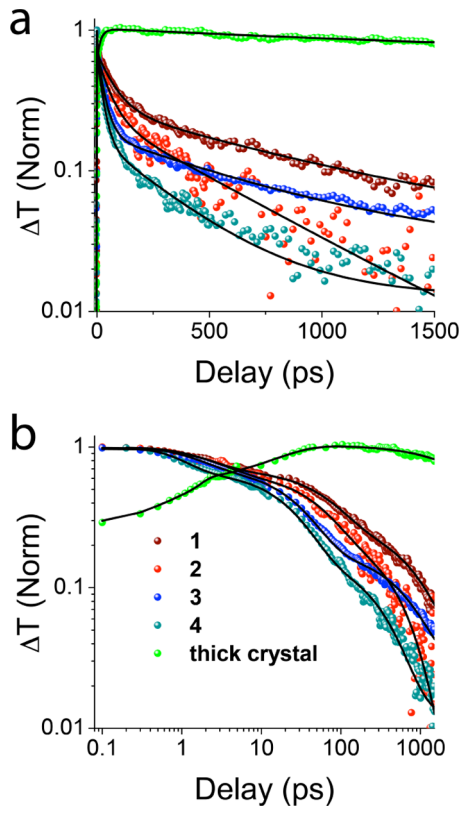

Figure 4. (a) Transient absorption dynamics with pump wavelength of 387 nm and a probe wavelength of 670 nm for positions 1, 2, 3, and 4. Exciton dynamics in the bulk is probed at 690 nm. The solid lines are fits of a triexponential decay function convoluted with a Gaussian response function. (b) same data as in part a but presented in a log−log scale.

We first consider intraband relaxation. In our experiments, excitons were created at the C excitonic level and probed at the A excitonic level. The rise time of the transient absorption signal reflects the time needed for photoexcited excitons to relax from the C excitonic level to the A excitonic level. We note here that hot carriers can also bleach the A exciton transitions; however, they are much less efficient in doing so than the excitons.[34] Transient absorption signals from both the monolayer and few-layer samples appear instantaneously within the experimental time resolution (~500 fs), implying a rapid intraband relaxation time of <500 fs. On the contrary, a significantly slower rise time in the thick crystal was observed indicating much slower intraband relaxation as clearly illustrated in Figure 4b. In semiconductors, intraband relaxation generally occurs through a sequence of carrier−carrier scattering and carrier−phonon scattering events.[30] Here we assign the fast rise time constant of ~2 ps observed in the thick crystal to carrier−carrier scattering and the slower rise time constant of ~20 ps to carrier−phonon scattering. A carrier−phonon scattering time of 20 ps for a 3.2 eV pump and a 1.9 eV probe indicates a carrier−phonon scattering rate of 0.065 eV/ps in bulk MoS_2.

TABLE 1. Fitting Parameters for Decay Curves in Figure 4 Using a Gaussian Response Function Convoluted with the Three-Exponential Decays Function of $Ae^{-t/\tau_1} + Be^{-t/\tau_2} + Ce^{-t/\tau_3}$

	τ_1 (ps)	τ_2 (ps)	τ_3 (ps)
1 (suspended monolayer)	2.6 ± 0.1 (39%)	74 ± 3 (39%)	850 ± 48 (22%)
2 (supported monolayer)	3.3 ± 0.2 (40%)	55 ± 3 (38%)	469 ± 26 (22%)
3 (suspended few-layer)	2.1 ± 0.1 (40%)	34 ± 1 (47%)	708 ± 55 (13%)
4 (supported few-layer)	1.2 ± 0.1 (47%)	29 ± 2 (41%)	344 ± 28 (12%)
thick crystal	1.8 ± 0.6 (19%) (rise)	20 ± 2 (81%) (rise)	2626 ± 192 (100%) (decay)

As signified by the instantaneous rise, the intraband relaxation rates in the monolayer and the few-layer positions are enhanced by a factor of more than 40 (<500 fs *versus* 20 ps) compared to that in the thick MoS_2 crystal. Similar enhancement in intraband relaxation channels has been observed previously with colloidal semiconducting quantum dots in comparison to their bulk counterparts. Nonphonon mechanisms such as defect scattering and Auger-type electron−hole energy transfer have been invoked because carrier−phonon coupling is similar in both quantum dots and the bulk and cannot explain the enhanced intraband relaxation.[22,24−27] To explain the dramatic enhancement in the intraband relaxation rate observed in monolayer and few-layer MoS_2, we consider both mechanisms. Auger-type electron−hole energy in semiconducting quantum dots occurs through confinement-enhanced energy transfer of the electron excess energy to a hole, with subsequent fast hole relaxation through its dense spectrum of states.[24−26] However, the effective masses and density of states for the electrons and holes are similar in MoS_2,[9,16] and Auger-type electron−hole energy transfer cannot account for the enhanced intraband relaxation observed in monolayer and few-layer cases.

The other and more likely process in monolayer and few-layer MoS_2 is that high energy carriers can thermalize by coupling to nearby traps or interfacial defects as proposed by Sercel for semiconductor quantum dots.[11,22] In such a model, the defect acts as an "elevator" carrying the electron from the upper level in the quantum dot to the lower level, providing an additional cooling channel and accelerating intraband carrier relaxation.[19,22] For monolayer MoS_2, essentially all atoms are on the surface or at the interface, hence the number of surface and interfacial defects per atom is greatly enhanced compared to the thick crystal, thus increasing the probability of the defect scattering processes. Therefore, we assign the fast intraband relaxation in monolayer and few-layer MoS_2 to defect-assisted carrier cooling. Possible defects in 2D crystals such as monolayer and few-layer MoS_2 include dislocation, vacancies, and edges as well as absorbate. For instance, these defects have been directly imaged in graphene by high resolution TEM.[35] To conclusively assign the nature of the defect sites in monolayer and few-layer MoS_2, correlated high-resolution TEM- transient absorption imaging measurements are needed. These measurements are currently underway.

Next we discuss the relaxation processes that account for the decays after the carriers relax to the A excitonic level. A single exponential decay of ~2.6 ns is observed following the initial rise in the thick crystal. Because the dynamics were probed at the A exciton and electron−hole recombination occurs at the lower energy indirect band gap, we tentatively attribute the ~2.6 ns decay to intervalley scattering (A exciton to indirect gap) in bulk MoS_2. To further assign this process, direct probing at the indirect gap will be helpful. Electron−hole recombination at the indirect band gap should be slower than the intravalley scattering as indicated by the nonzero background at the long decay time. Owing to the limit of our time window (~4 ns), the time scale of the indirect electron−hole recombination cannot be accurately determined. Recombination in bulk indirect semiconductors such as silicon is on the order of microseconds to milliseconds.[2,3,36]

For the monolayer and few-layer regions, the overall decay is significantly faster than that of the bulk. Interband electron−hole recombination is expected to be faster for the monolayer, because the energy of the indirect band gap of MoS_2 increases as thickness decreases, and the material ultimately becomes a direct band gap semiconductor at the monolayer level.[11] The excited state population decay observed in monolayer and few-layer samples is multiexponential with three distinct time scales, namely a fast decay (τ_1) of 2−4 ps, an intermediate decay (τ_2) of 30−80 ps, and a slow decay (τ_3) of 300−1000 ps. The multiexponential nature implies that more than one relaxation process is involved. The fast decay was extremely rapid and did not exhibit a strong dependence on pump fluence, therefore we ruled out exciton−exciton annihilation. This fast decay time is similar to the fast decay component observed in the PL lifetime measurements.[17] We tentatively assign the fast decay of 2−4 ps to trapping of the excitons by surface trap states. The fast trapping is consistent with the low quantum yield (on the order of 10^{-3}) observed even in monolayer MoS_2 that exhibits the strongest PL intensity.[11] Previous work on MoS_2 nanoclusters proposed that both shallow and deep traps exist.[37] The exact nature and the depth of the traps require a further temperature-dependent study, which is currently underway.

The intermediate decay time constant (τ_2) is similar to the interband carrier-phonon scattering time observed in recent photoluminescence lifetime measurements, which was found to be strongly dependent on temperature.[17] τ_2 in both monolayer and few-layer structures is slower than the intraband carrier-phonon scattering time of ~20 ps found in the bulk due to the interband nature, but overall on the same time scale, indicating the strength of carrier-phonon coupling is not significantly altered by quantum confinement effects.

The slowest decay component (τ_3) observed in monolayer and few-layer cases on the order of hundreds of picoseconds is assigned to a direct interband electron−hole recombination. This recombination is significantly faster than the indirect recombination time in the bulk. The faster electron−hole recombination in the monolayer can be explained by its direct band gap nature.[11,38] Suspended few-layer ($N \approx 4$) structures had similar τ_3 values as the monolayer, suggesting that few-layer MoS_2 are also direct

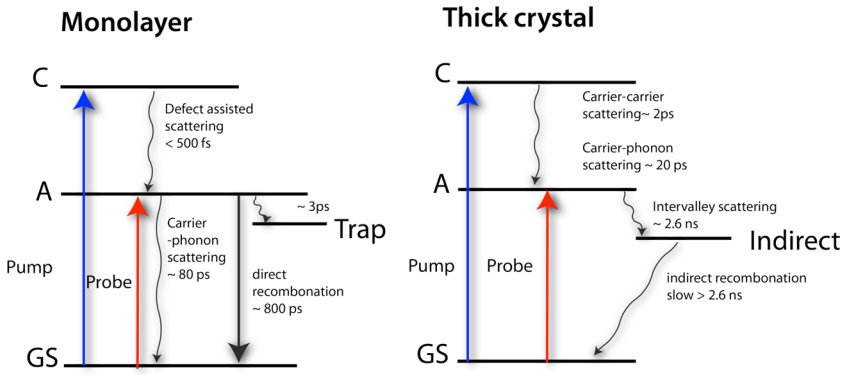

Figure 5. Schematic summary of relaxation processes in monolayer and thick MoS_2 crystal.

semiconductor like. This agrees with an appreciable direct band gap PL from the A exciton observed in few-layer ($N = 2-6$) cases, albeit with lower quantum yield than in the monolayer.[10,11]

Another possible mechanistic explanation for τ_3 is exciton/carrier diffusion since the probe volume is small.[19] However, mobility of as exfoliated MoS_2 is low, on the order of ~1 $cm^2/(V\ s)$ and corresponding to diffusion coefficient of 0.025 cm^2/s at room temperature using the Einstein relation.[2,3] A diffusion distance of 16 nm given by the diffusion coefficient and an average exciton lifetime of 100 ps (as defined by the 1/*e* value), imply less than 6% of carriers diffuse out of the probe spot size of 400 nm. We therefore conclude that carrier diffusion does not significantly contribute to our observations.

Finally we compare our results to previous steady state PL measurements. The PL quantum yield is enhanced in the suspended regions compared to the substrate-supported region.[11] Our measurements show that the supported regions have faster τ_3 decays than the suspended regions (~400 ps *versus* ~800 ps), suggesting the Si_3N_4 substrate can depopulate the excited states. Possible depopulation mechanisms involving substrates include energy or charge transfer to the substrate. This is consistent with the enhanced PL efficiency for a suspended MoS_2 monolayer.[11] However, the difference in dynamics for the suspended and supported areas might not be as big as previous PL work[11] would have suggest. This can be explained by two reasons: (1) Nonradiative rather than radiative relaxation pathways dominate the transient absorption dynamics in both the suspended and substrate supported areas. The quantum yield is low on the order of $\sim 10^{-3}$ even in the suspended monolayer MoS_2 with the strongest PL intensity. (2) A quantitative conclusion is hard to draw from comparing data across laboratories. The dominating nanoradiative pathway is defect related as discussed earlier. The samples used in different laboratories can have very different conditions with respect to the nature of defects and defect density.

CONCLUSION

We have performed a transient absorption spectroscopic investigation of exciton dynamics in monolayer and few-layer MoS_2 2D crystals at room temperature. Figure 5 presents a schematic summary of the relaxation processes for both monolayer and thick MoS_2 crystal. Exciton dynamics in monolayer and few-layer cases deviate significantly from those in the thick crystal, demonstrating the importance of quantum confinement effects and surface defects in modulating relaxation pathways. While carrier−carrier (~2 ps) and carrier−phonon scattering (~20 ps) dominated intraband relaxation in the thick crystal, the dramatically enhanced intraband relaxation time (<500 fs) observed in monolayer and few-layer was attributed to defects-assisted intraband scattering. Exciton recombination dynamics of the monolayer and few-layer cases were described by triexponential decay functions with characteristic times of a few picoseconds, tens of picoseconds, and hundreds of picoseconds. The fast trapping of excitons by surfaces defects was observed to be on the order of 2−4 ps, signifying the importance of defects in modulating relaxation pathways. The intermediate decay component of tens of picoseconds was attributed to carrier−phonon scattering. Consistent with an indirect−direct crossover at the monolayer due to quantum confinement effects, faster interband electron−hole combination times of hundreds of picoseconds were observed in monolayer and few-layer samples as compared to nanoseconds or longer in the thick crystal. Our experiments suggest that nonradiative rather than radiative relaxation pathways dominate the dynamics in monolayer and few-layer MoS_2 crystals.

EXPERIMENTAL METHODS

Ultrathin MoS_2 films were fabricated from bulk crystals of molybdenite (SPI) by mechanical exfoliation. Flakes of monolayer and few-layer MoS_2 were first deposited onto SiO_2/Si wafers coated with polyvinyl(PVA) and polymethyl methacrylate(PMMA). After identification with an optical microscope,[20] monolayer

and few-layer MoS_2 films were transferred onto previously patterned target substrates. A schematic drawing of the cross-section of the patterned substrate is shown in Supporting Information, Figure S3. The substrate is a Si wafer with a 60 nm thick SiO_2 layer and a 20 nm thick Si_3N_4 layer. Holes with a diameter of 1.2 μm are defined on the front side by electron beam lithography followed by dry etching of Si_3N_4. Silicon is selectively back-etched with KOH, leaving a patterned 20 nm thick Si_3N_4 membrane at the front side.

Microtransient absorption spectroscopy and imaging setup was base on a Ti:sapphire oscillator (Coherent Mira 900) that pumps an optical parametric oscillator (Coherent Mira OPO) and is coupled to an inverted optical microscope (Nikon Ti-U). A schematic of the experimental setup is shown in Supporting Information, Figure S4. All measurements presented in this manuscript were carried out at room temperature. Output from the Ti:sapphire oscillator at 775 nm was split into two beams, one of which (70% of the output) was used to pump the OPO and served as the probe. The second harmonic of the rest (30%) of the Ti:sapphire output provided the pump beam. The polarizations of the pump and probe beams were made parallel, the beams were focused at the sample with a 60×, 0.9 numerical aperture (NA), and the pump and probe beams were spatially overlapped at the sample. The transmitted beams were collected by another 60×, 0.9 NA objective, and the probe was detected with an avalanche photodiode (APD, Hamamatsu C5331-04).

Pump-induced changes in the probe transmission (ΔT) were measured by modulating the pump beam at 3 MHz with an acousto-optic modulator (AOM, Gooch and Housego), and the output of the APD was monitored with a lock-in amplifier (Zurich Instrument). Such high frequency modulation is necessary for achieving shot noise limited detection.[39] Transient absorption traces were obtained by delaying the probe with respect to the pump with a mechanical translation stage (Thorlabs). The time-resolution at the sample was *ca.* 500 fs. Transient absorption images at a fixed pump−probe delay were acquired by raster scanning the beams with a pair of galvanometer mirrors (Thorlabs), and recording the change in transmission of the probe ΔT. The spatial resolution is ~0.4 μm in transient absorption microscopy images. Microtransient absorption spectra of fix positions and fix delay time are constructed by scanning the probe wavelength with the OPO. Shot noise limit in our experiment is calculated to be 8×10^{-8} with an integration time of 120s and a pump fluence of 3.7 uJ/cm^2 at 670 nm.

Ground-state absorption spectra were acquired with the same inverted microscope equipped with an optical spectrograph (Andor Technology) and a TE cooled CCD (Andor Technology). A 60×, 0.9 NA microscope objective was used to focus a halogen white light source. The spot size of the white light is ~1 μm. Reflected light was collected by the same objective and subsequently detected by the spectrograph and CCD combination (Andor Technology). Reflected light was collected by the same objective and subsequently detected by the spectrograph and CCD combination (Andor Technology). Background subtraction is achieved by using reflected spectrum from a bare area on the same substrate as a reference.

Raman spectra were collected by a Renishaw Raman microscope (RM1000) equipped with an argon-ion laser at 514 nm as an excitation source. The excitation beam was focused by a 50×, 0.75NA objective, and the Raman scattered light was collected with the same objective.

Conflict of Interest: The authors declare no competing financial interest.

Acknowledgment. L. Huang and B. Gao acknowledge the support of the Division of Chemical Sciences, Geosciences and Biosciences, Basic Energy Sciences, Office of Science, United States Department of Energy through Grant No. DE-FC02-04ER15533. H. Shi acknowledges support from the Sustainable Energy Initiative of the University of Notre Dame. D. Jena and H. G. Xing acknowledge support from the Air Force Office of Scientific Research (FA9550-12-1-0257) and National Science Foundation (NSF-ECCS 1232191). H. G. Xing also acknowledges the support from a NSF CAREER award. S. Bertolazzi, J. Brivio, and A. Kis acknowledge the support from Swiss National Science Foundation (Grant No. 200021_132102), the Swiss Nanoscience Institute (NCCR Nanoscience) and European Research Council (Grant No. 240076). Si_3N_4 membrane fabrication was carried out in part in the EPFL Center for Micro/Nanotechnology (CMI). This publication is contribution No. NDRL 4933 from the Notre Dame Radiation Laboratory.

Supporting Information Available: Figures S1−S6, and Table S1 as described in the text. This material is available free of charge *via* the Internet at http://pubs.acs.org.

REFERENCES AND NOTES

1. Yoffe, A. Layer Compounds. *Annu. Rev. Mater. Sci.* **1973**, *3*, 147–170.
2. Novoselov, K.; Jiang, D.; Schedin, F.; Booth, T.; Khotkevich, V.; Morozov, S.; Geim, A. Two-Dimensional Atomic Crystals. *Proc. Natl. Acad. Sci. U.S.A.* **2005**, *102*, 10451–10453.
3. Radisavljevic, B.; Radenovic, A.; Brivio, J.; Giacometti, V.; Kis, A. Single-Layer MoS_2 Transistors. *Nat. Nanotechnol.* **2011**, *6*, 147–150.
4. Ramakrishna Matte, H.; Gomathi, A.; Manna, A. K.; Late, D. J.; Datta, R.; Pati, S. K.; Rao, C. MoS_2 and WS_2 Analogues of Graphene. *Angew. Chem.* **2010**, *122*, 4153–4156.
5. Radisavljevic, B.; Whitwick, M. B.; Kis, A. Integrated Circuits and Logic Operations Based on Single-Layer MoS_2. *ACS Nano* **2011**, *5*, 9934–9938.
6. Zhang, Y.; Ye, J.; Matsuhashi, Y.; Iwasa, Y. Ambipolar MoS_2 Thin Flake Transistors. *Nano Lett.* **2012**, *12*, 1136–1140.
7. Lebègue, S.; Eriksson, O. Electronic Structure of Two-Dimensional Crystals From *ab Initio* Theory. *Phys. Rev. B* **2009**, *79*, 115409.
8. Kuc, A.; Zibouche, N.; Heine, T. Influence of Quantum Confinement on the Electronic Structure of the Transition Metal Sulfide TS2. *Phys. Rev. B* **2011**, *83*, 245213.
9. Cheiwchanchamnangij, T.; Lambrecht, W. R. Quasiparticle Band Structure Calculation of Monolayer, Bilayer, and Bulk MoS_2. *Phys. Rev. B* **2012**, *85*, 205302.
10. Zeng, H.; Liu, G. B.; Dai, J.; Yan, Y.; Zhu, B.; He, R.; Xie, L.; Xu, S.; Chen, X.; Yao, W. Optical Signature of Symmetry Variations and Spin-Valley Coupling in Atomically Thin Tungsten Dichalcogenides. *arXiv:1208.5864* **2012**.
11. Mak, K.; Lee, C.; Hone, J.; Shan, J.; Heinz, T. Atomically Thin MoS_2: A New Direct-Gap Semiconductor. *Phys. Rev. Lett.* **2010**, *105*, 136805.
12. Splendiani, A.; Sun, L.; Zhang, Y.; Li, T.; Kim, J.; Chim, C.-Y.; Galli, G.; Wang, F. Emerging Photoluminescence in Monolayer MoS_2. *Nano Lett.* **2010**, *10*, 1271–1275.
13. Mak, K. F.; He, K.; Shan, J.; Heinz, T. F. Control of Valley Polarization in Monolayer MoS_2 by Optical Helicity. *Nat. Nanotechnol.* **2012**, *7*, 494–498.
14. Zeng, H.; Dai, J.; Yao, W.; Xiao, D.; Cui, X. Valley Polarization in MoS_2 Monolayers by Optical Pumping. *Nat. Nanotechnol.* **2012**, *7*, 490–493.
15. Frindt, R. Optical Absorption of a Few Unit-Cell Layers of MoS_2. *Phys. Rev.* **1965**, *140*, A536–A539.
16. Fortin, E.; Raga, F. Excitons in Molybdenum Disulphide. *Phys. Rev. B* **1975**, *11*, 905–912.
17. Korn, T.; Heydrich, S.; Hirmer, M.; Schmutzler, J.; Schueller, C. Low-Temperature Photocarrier Dynamics in Monolayer MoS_2. *Appl. Phys. Lett.* **2011**, *99*, 102109.
18. Wang, R.; Ruzicka, B. A.; Kumar, N.; Bellus, M. Z.; Chiu, H.-Y.; Zhao, H. Optical Pump-Probe Studies of Carrier Dynamics in Few-Layer MoS_2 American Physical Society, APS March Meeting, 2012.
19. Wang, R.; Ruzicka, B.; Kumar, N.; Bellus, M. Ultrafast and Spatially Resolved Studies of Charge Carriers in Atomically Thin Molybdenum Disulfide. *Phys. Rev. B* **2012**, *86*, 045406.
20. Benameur, M. M.; Radisavljevic, B.; Héron, J. S.; Sahoo, S.; Berger, H.; Kis, A. Visibility of Dichalcogenide Nanolayers. *Nanotechnology* **2011**, *22*, 125706.
21. Bertolazzi, S.; Brivio, J.; Kis, A. Stretching and Breaking of Ultrathin MoS_2. *ACS Nano* **2011**, *5*, 9703–9709.

22. Schroeter, D.; Griffiths, D.; Sercel, P. Defect-Assisted Relaxation in Quantum Dots at Low Temperature. *Phys. Rev. B* **1996**, *54*, 1486–1489.
23. Lee, C.; Yan, H.; Brus, L. E.; Heinz, T. F.; Hone, J.; Ryu, S. Anomalous Lattice Vibrations of Single- and Few-Layer MoS_2. *ACS Nano* **2010**, *4*, 2695–2700.
24. Klimov, V.; McBranch, D. Femtosecond 1P-to-1S Electron Relaxation in Strongly Confined Semiconductor Nanocrystals. *Phys. Rev. Lett.* **1998**, *80*, 4028–4031.
25. Klimov, V.; McBranch, D.; Leatherdale, C.; Bawendi, M. Electron and Hole Relaxation Pathways in Semiconductor Quantum Dots. *Phys. Rev. B* **1999**, *60*, 13740.
26. Klimov, V.; Mikhailovsky, A.; McBranch, D.; Leatherdale, C.; Bawendi, M. Mechanisms for Intraband Energy Relaxation in Semiconductor Quantum Dots: The Role of Electron–Hole Interactions. *Phys. Rev. B* **2000**, *61*, R13349–R13352.
27. El-Sayed, M. A. Small Is Different: Shape-, Size-, and Composition-Dependent Properties of Some Colloidal Semiconductor Nanocrystals. *Acc. Chem. Res.* **2004**, *37*, 326–333.
28. Evans, B.; Young, P. Exciton Spectra in Thin Crystals. *Proc. R. Soc. London, Ser. A* **1967**, *298*, 74–96.
29. Consadori, F.; Frindt, R. Crystal Size Effects on the Exciton Absorption Spectrum of WSe_2. *Phys. Rev. B* **1970**, *2*, 4893–4896.
30. Shah, J. Ultrafast Studies of Carrier Relaxation in Semiconductors and Their Microstructures. *Superlatt. Microstruct.* **1989**, *6*, 293–302.
31. Shah, J. *Ultrafast Spectroscopy of Semiconductors and Semiconductor Nanostructures*, 2nd ed.; Springer: New York, 1999.
32. Ostojic, G. N.; Zaric, S.; Kono, J. Stability of High-Density One-Dimensional Excitons in Carbon Nanotubes Under High Laser Excitation. *Phys. Rev. Lett.* **2005**, *94*, 097401.
33. Kim, J.-Y.; Choi, S.-M.; Seo, W.-S.; Cho, W.-S. Thermal and Electronic Properties of Exfoliated Metal Chalcogenides. *Bull. Korean Chem. Soc.* **2010**, *31*, 3225–3227.
34. Schmitt-Rink, S.; Chemla, D.; Miller, D. Theory of Transient Excitonic Optical Nonlinearities in Semiconductor Quantum-Well Structures. *Phys. Rev. B* **1985**, *32*, 6601–6609.
35. Meyer, J. C.; Kisielowski, C.; Erni, R.; Rossell, M. D.; Crommie, M. F.; Zettl, A. Direct Imaging of Lattice Atoms and Topological Defects in Graphene Membranes. *Nano Lett.* **2008**, *8*, 3582–3586.
36. Kovalev, D.; Heckler, H.; Ben-Chorin, M.; Polisski, G.; Schwartzkopff, M.; Koch, F. Breakdown of the K-Conservation Rule in Si Nanocrystals. *Phys. Rev. Lett.* **1998**, *81*, 2803–2806.
37. Doolen, R.; Laitinen, R.; Parsapour, F.; Kelley, D. F. Trap State Dynamics in MoS_2 Nanoclusters. *J Phys. Chem. B* **1998**, *102*, 3906–3911.
38. Sykora, M.; Mangolini, L.; Schaller, R. D.; Kortshagen, U.; Jurbergs, D.; Klimov, V. I. Size-Dependent Intrinsic Radiative Decay Rates of Silicon Nanocrystals at Large Confinement Energies. *Phys. Rev. Lett.* **2008**, *100*, 067401.
39. Chong, S.; Min, W.; Xie, X. S. Ground-State Depletion Microscopy: Detection Sensitivity of Single-Molecule Optical Absorption at Room Temperature. *J. Phys. Chem. Lett.* **2010**, *1*, 3316–3322.